CHAPTER 5

Effects of Vanadium Doping on the Structural and Electronic Properties of $CuCoO_2$

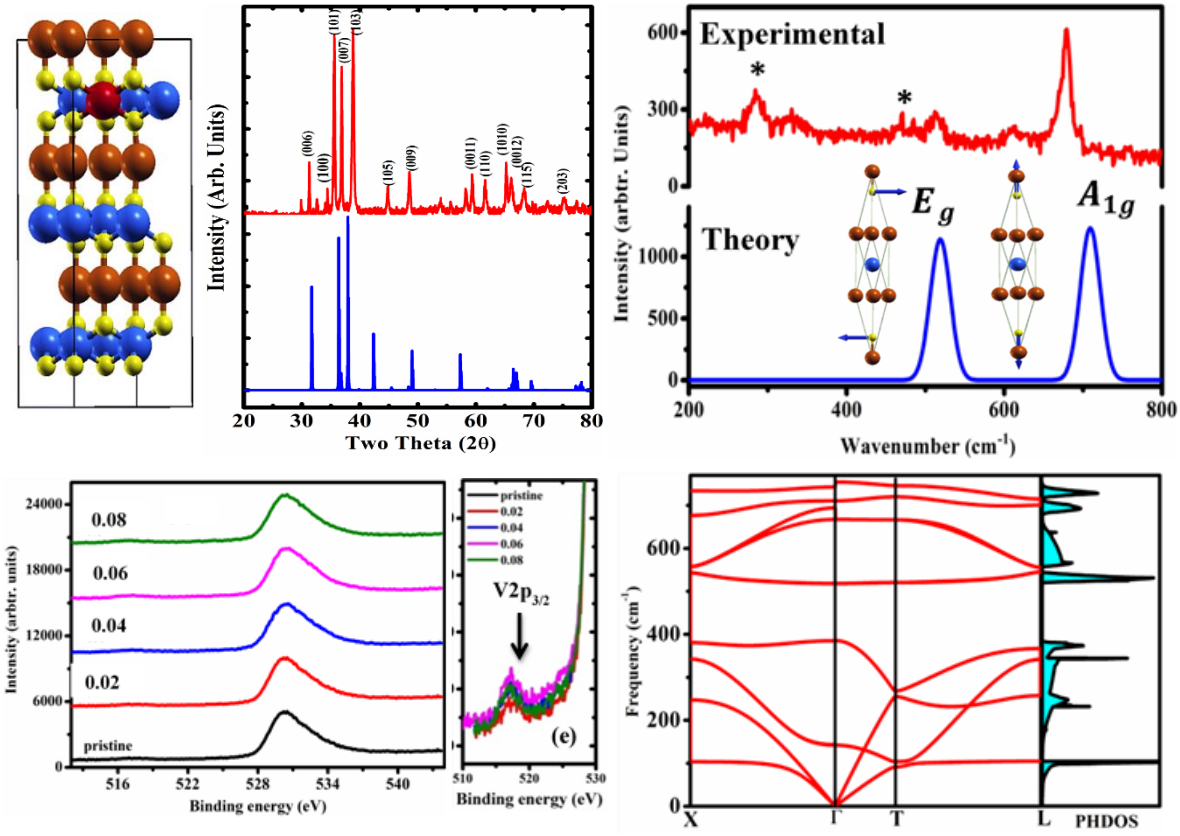

D. Upadhyay, A. Pratap, P. K. Jha "Effects of vanadium doping on the structural and electronic properties of $CuCoO_2$" *(In Communication)*

5.1 Introduction

The exploration of novel energy resources with new improvements is a crucial problem in modern society. Delafossite-type oxides such as $CuMO_2$ (M = trivalent cation) exhibit potential to be utilized in renewable energy sources such as thermoelectric devices [1], dye-sensitized solar cell (DSSC's) [2], catalysts for water splitting [3], etc. due to their layered structural geometry. The atomic arrangements and their atomic coordination deliver remarkable applicability in electronic applications and stability at extreme conditions such as high pressure and temperature [4]. Apart from these applications, delafossites have curious physical properties suitable for fundamental as well as technological applications. In recent times, delafossites are being used as p-type transparent conducting materials, however, the conductivity of these materials is still low as compared to n-type semiconductors [5, 6]. The low electrical conductivity creates a barrier in the development of technologies that necessitate both p and n-type semiconductors. Enormous research is being conducted for the enhancement of conductivity of these materials without compromising transparency [7-9]. In delafossite type materials, the mobile charge carrier holes are responsible for p-type conductivity. In these oxides, the holes are generally localized around O 2p orbitals because of the electronegative character of O atoms. Further, the O 2p orbitals are far lower-lying than the valence orbital of metallic atoms that is responsible for the formation of deep acceptor level. These holes require high energy to overcome a large barrier height to migrate within the crystal lattice, resulting in poor electrical conductivity and low hole mobility. To overcome the barrier, recent researches are being dedicated to the doped Al, Cu and Ga based delafossites [10, 11]. Very recently, highest conductivity is reported for the Mg-doped $CuCrO_2$ [8]. The p-type conductivity is affected by the high hole effective mass as well as low hole mobilities in p-type delafossites similar to Cu_2O. It may be caused by the lack of Cu–O–Cu bonds as seen in Cu_2O [12]. Higher conductivity was detected for $CuCrO_2$ and $CuFeO_2$ due to favorable mixing of metal and

oxygen [12, 13]. The electronic bands near the Fermi level were accomplished by hole doping into a wide gap of Cu^{+} oxide, with the d^{10} closed shell. Hence, the top of the valence band was expected to have the Cu 3d character with some O 2p due to hybridization. The conductivity of these oxides depends on the p-d hybridization; the suitable combination of monovalent and trivalent cations can give interesting results on the conductivity and transparency of delafossite oxides.

It is well recognized that the doping of trivalent or divalent metals in delafossite type oxides significantly enhances the conductivity of these oxides [8, 11]. Different investigations have been performed to describe the behavior of conductivity by doping of different cations. The extraordinary electrical conductivity is a consequence of decrease in the ionic radius of the M^{III} cation [8, 14]. Small ionic radii of trivalent cations result in the reduction in lattice parameters increases metal-oxygen overlap. The metal-oxygen overlap generates more delocalized holes that are good for small hole effective mass and higher hole mobility. Doping of transition metals significantly modulates the valence band maximum (VBM) in delafossites resulting in the low hole effective mass. A detailed analysis of electronic properties is required to explore the influence of transition metal (M^{III}) cations. In the present work, we have studied the influence of V doping at the Co site of the $CuCoO_2$ both experimentally and theoretically. The x-ray diffraction (XRD) and x-ray photoelectron spectroscopy (XPS) techniques have been used to examine the crystal geometry and valence state along with the bonding nature of these compounds [17, 18]. Further, the observed experimental findings have been analysed with the density functional theory (DFT) [20]. The magnetic properties have also been analyzed by the vibrating sample magnetometer (VSM) and the results are correlated with the spin polarized DFT calculations.

5.2 Methodology

5.2.1 Sample Preparation and Characterization

Samples of pristine $CuCoO_2$ and vanadium (V) doped $CuCo_{1-x}V_xO_2$ (x= 0.02, 0.04, 0.06, 0.08) were prepared by taking the stoichiometric weight of high purity Cu_2O, Co_3O_4 and V_2O_5 and mixed homogeneously using a wet mixing technique. After drying the mixture in the powder form, they were filled in alumina crucibles. The mixrture was heated to 1273 K for 24 h and then allowed to cool to reach room temperature. The structure of the samples was analyzed by the x-ray diffraction (XRD) measurements using a 1D PSD detector (LynxEye) with $Cu\ K_\alpha$ radiation. Raman measurements were performed using micro-Raman model STR 500 with Nd-YAG laser as a source with 532 nm wavelength and Peltier cooled CCD detector. The elemental compositions and bonding nature are analyzed by XPS using Specs, Phoibos 225 (0–15 keV) spectrometer with $Al\ K_\alpha$ radiation (1486.6 eV), detector MCP with CCD (Peltier-cooled) and 60 meV spectrometer resolution at 300 K. Magnetic properties are characterized by the vibrating sample magnetometer (EG & G Model PAR 155) at 300 K.

5.2.2 Computational Details

The ground state structural properties of pristine and V doped $CuCoO_2$ were studied by density functional theory (DFT) based first-principles calculations encoded in the Quantum Espresso package [20]. Generalized gradient approximation (GGA) functionals including spin polarization were used for the exchange-correlation functional [21] in which the energy was parameterized by Perdue, Burke, and Ernzerhof (PBE) within norm-conserving pseudopotentials. The V-doped $CuCoO_2$ system has been modeled by considering the 2×2×1 supercell with 48 atoms, in which a cobalt (Co) atom was replaced by a V atom. The energy cut-off for the wave function and charge density used was 80 Ry and 320 Ry, respectively. For integral calculations in reciprocal lattice, we used 8×8×8 k-point grids in the Monkhorst–Pack

scheme [22] for the 2×2×1 supercell. Structural optimization was carried out using the Broyden−Fletcher−Goldfarb−Shanno (BFGS) algorithm imposing the force and energy convergence threshold of 0.001 eV/Å and 10^{-10} Ry to minimize the internal force and energy, respectively. The calculations of vibrational properties were executed by employing the density functional perturbation theory (DFPT) [23].

5.3 Results and Discussion

5.3.1 Structural Properties

The delafossite compounds related to a family of ternary oxides are generally characterized as $A^{+1}M^{+3}O_2$ (Where, A = Cu, Ag, Au, Pd, Pt; B = Cr, Fe, Co, Al, Ga). The delafossites comprise layered structures in which 'A' cation is stacked between edge-shared MO_6 octahedral layers and generally crystallize in the rhombohedral ($R\bar{3}m$) or hexagonal ($P6_3/mmc$) symmetries. The rhombohedral crystal geometry of $CuCoO_2$ is shown in Fig. 5.1 (a). As shown in Fig. 5.1(a), the delafossite $CuCoO_2$ consists layered structure in which monovalent cations Cu^{+1} has linearly coordinated with oxygen O^{-2} atoms and octahedrally surrounded by six O^{-2} atoms with a trivalent cation Co^{+3}. Further, the O^{-2} is bonded with three equivalent Co atoms and one Cu atom to form a mixture of distorted edge-corner sharing $OCuCo_3$ trigonal pyramids. The x-ray diffraction measurements were also conducted to analyze the crystal structure of pristine $CuCoO_2$ (CCO) and V doped $CuCoO_2$ i. e. $CuCo_{1-x}V_xO_2$ (CCVO). The XRD patterns of CCO and CCVO samples are presented in Fig. 5.1(b-c). It can be seen from Fig. 5.1 that the diffraction peaks of as obtained CCO and CCVO samples are indexed to pure phase $CuCoO_2$ (JCPDS card No. 21-0256) as evident by the peak positions. Obtained XRD patterns of CCO samples have an inline agreement with the simulated XRD pattern (Fig. 5.1(b)).

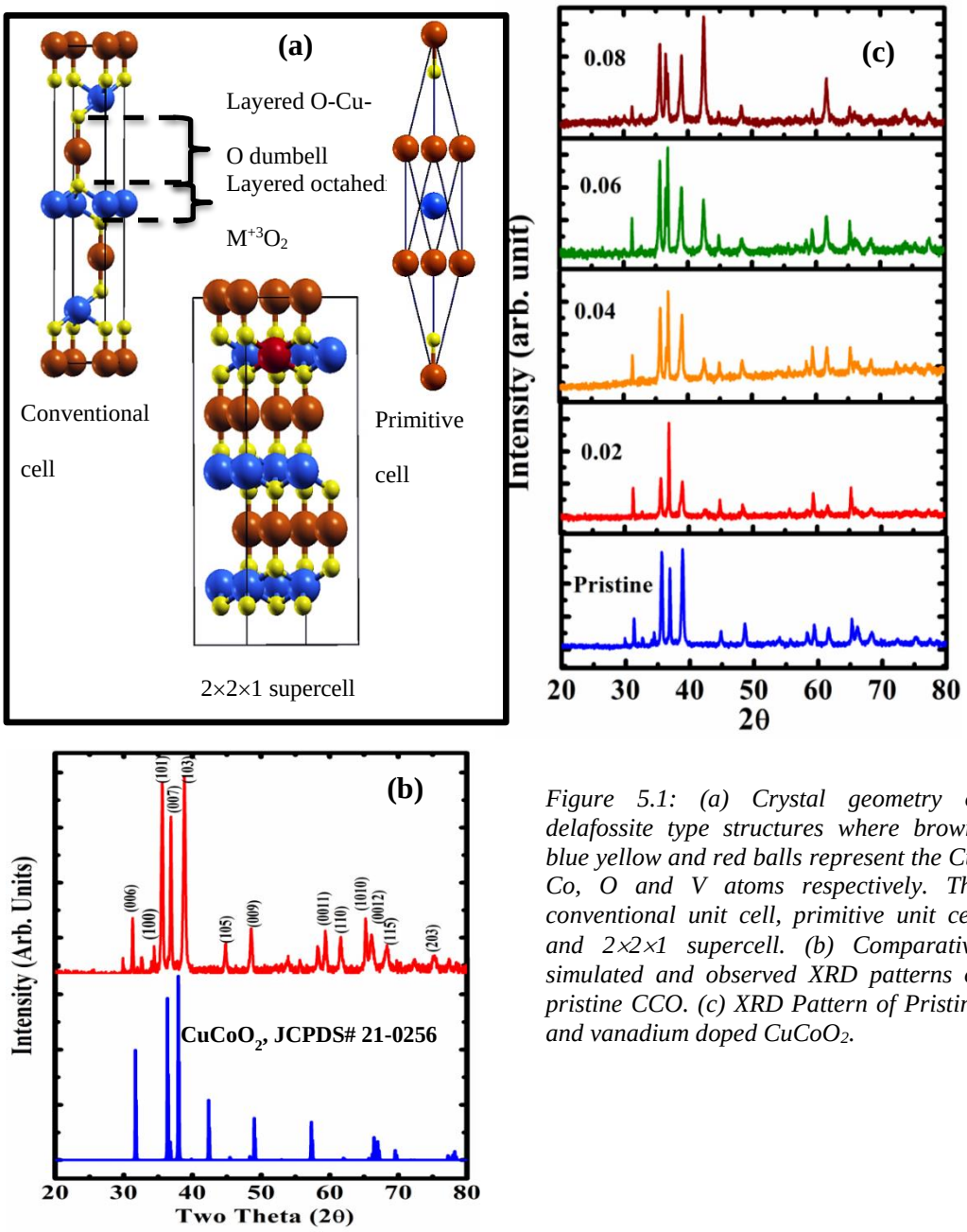

Figure 5.1: (a) Crystal geometry of delafossite type structures where brown, blue yellow and red balls represent the Cu, Co, O and V atoms respectively. The conventional unit cell, primitive unit cell and 2×2×1 supercell. (b) Comparative simulated and observed XRD patterns of pristine CCO. (c) XRD Pattern of Pristine and vanadium doped $CuCoO_2$.

The XRD patterns indicate the pure phase formation of CCO in rhombohedral geometries with the $R\bar{3}m$ (#166) space group and no impurity peaks are detected for the samples within the experimental limits. The obtained XRD patterns of CCO are compared with the previously reported XRD data that shows reasonable agreement in terms of the peak positions. Further, we have analyzed the effect of vanadium doping in CCO with different concentrations of

vanadium (0.02, 0.04, 0.06, and 0.08). It is well established that the dopant (V) is expected to prefer a valence state having radii closer to the parent element radius (Co^{3+} = 0.68 Å). A theoretical model based on density functional theory is adopted to simulate the V doped CCO, in which a 2×2×1 super-cell (see Fig. 5.1 (a)), is considered to correspond a ratio of 1:11, i.e. 8.3 wt% of V. We used these systems to evaluate the structural, electronic and magnetic properties of V doped CCO and understand the effect of vanadium substitution.

5.3.2 X-ray Photoelectron Spectroscopy (XPS) and Electronic Properties

The elemental chemical states of the pristine CCO and V doped CCO have been examined by X-ray photoelectron spectroscopy (XPS), as shown in Fig. 5.2 (a-e). The XPS survey spectra (Fig. 5.2(a)) of these samples are very similar, confirming the presence of Cu, Co, V and O elements in CCO and CCVO samples. This is also the case for the high-resolution spectra of each element. The wide survey of XPS spectra (Fig 5.2(a)) of CCO and CCVO show that four peaks located at 285.0, 530.7, and 964.2 eV are indexed to C 1s, O 1s, and O_{KLL}, respectively. The peaks located near 934.6 and 954.5 eV (Fig. 5.2 (b)) correspond to the binding energies (BE) of Cu^{+} $2p_{3/2}$ and Cu^{+} $2p_{1/2}$. These BE values agree with those in the literature [24-26] confirming the presence of Cu^{+} cations. There is also a satellite peak around 942.0 eV in Cu XPS spectra. The peaks near 781.0 and 795.4 eV (Fig. 5.2(c)) are illustrative of the BE of Co $2p_{3/2}$ and Co $2p_{1/2}$, which confirms the trivalent state of cobalt (Co^{3+}) in these CCO and CCVO compounds. Noticeably, the absence of any shift in Cu and Co XPS spectra (Fig. 5.2 (b-c)) indicates the dominance of Co^{3+} and Cu^{+} oxidation states during V doping. The above results demonstrate the existence of Co^{3+} in the crystal structure of CCO and CCVO. The O 1s curves (Fig. 5.2 (d)) show the BE peak at 530.0 eV that can be assigned to the BE of oxygen (O 1s) suggesting the metal-oxygen bonding. Also, the V $2p_{3/2}$ peak observed at 516.8 eV is related to the V^{4+} valence state.

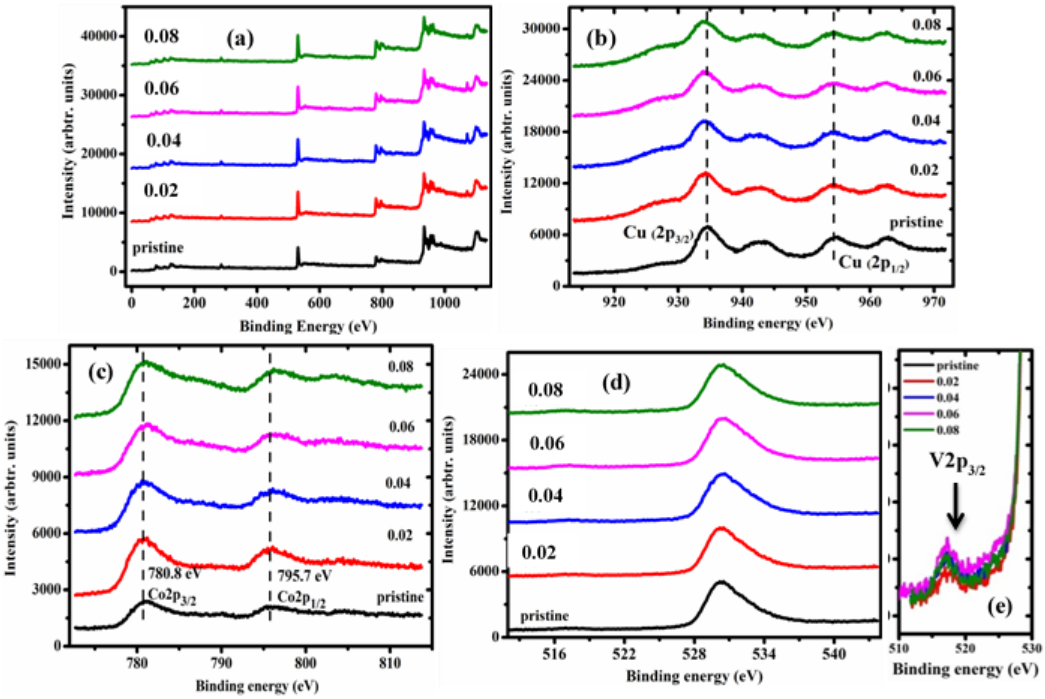

Figure 5.2: (a) Overall core level XPS spectra of the CCO and CCVO samples. (b) XPS spectra of the Cu 2p (c) Co 2p (d) O 1s and (e) V 2p.

To understand the electronic behavior of pristine CCO and V doped CCO, we have calculated the electronic band structures and projected density of states of these compounds using spin polarised density functional theory. It is clear from the XPS spectra that the Cu, Co, and V atoms are found in their monovalent, trivalent, and tetravalent valence states. The electronic band structure of CCO and CCVO compounds are shown in Fig. 5.3(a-b). It can be seen from Fig. 5.3(a) that the pristine CCO shows an indirect band gap of 1.03 eV. The band structure of pristine CCO is almost identical for the spin up and spin down channels. After 8.3% V doping, the band gap of CCO reduces to 0.40 eV, while the nature of band dispersion still remains indirect (Fig. 5.3(b)). To deeply understand the contribution of each atom in the electronic band structure and also to understand the effects of V doping on electronic properties, we have calculated the projected density of states (PDOS) and presented them in Fig. 5.3(c-d). It can be seen from the Fig. 5.3(c) that the valence band maximum (VBM) is constructed by the major contributions of Cu 3d orbitals, while the conduction band minimum shows the major contributions of Co 3d orbitals. The O 2p orbitals are projected in a deep valence band, after

the major peaks of Cu and Co d orbitals. The low lying O 2p contribution is responsible for the low electrical conductivity of these oxides. It is well known that the electronegative nature of O attracts the positively charged holes in p-type semiconductors and the O 2p orbitals placed in deep valence bands (Fig. 5.3(c)).

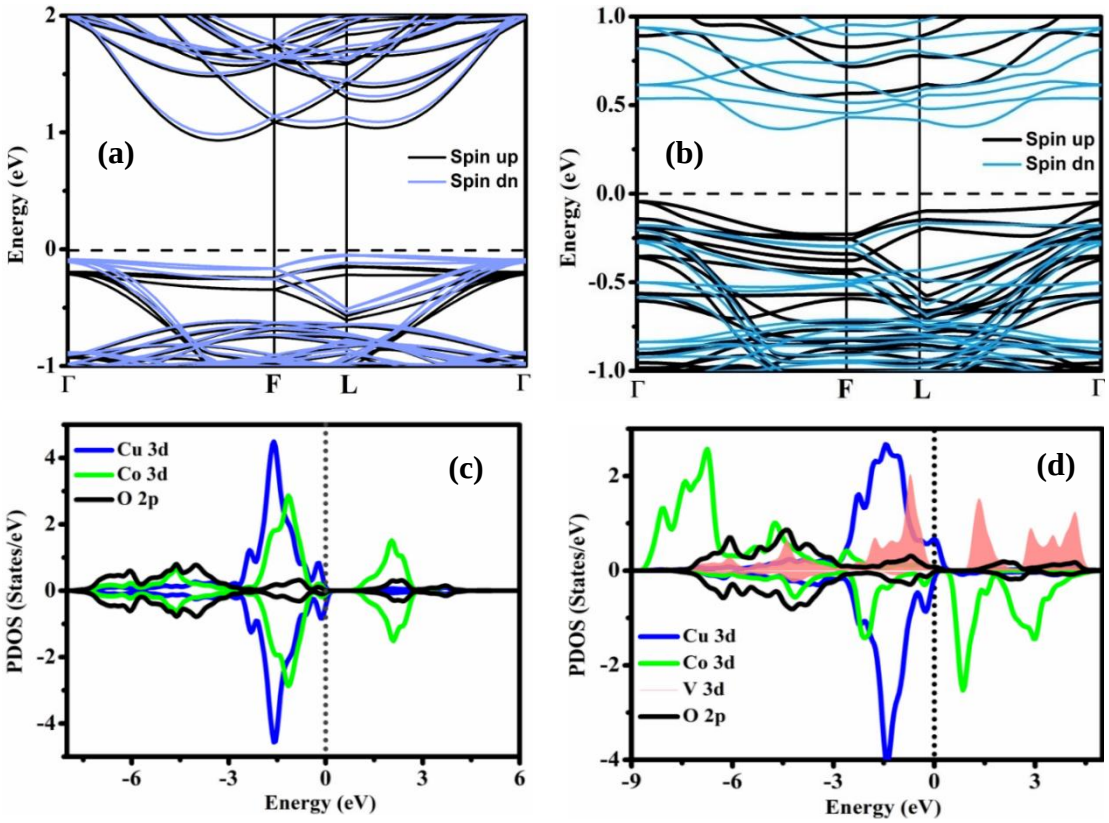

Figure 5.3: (a) Spin polarised electronic band structures of pristine CCO (b) V doped CCVO (0.08) (c) Projected density of states (PDOS) of CCO (d) V doped CCO compounds.

The major contributions of metal (Cu) 3d orbitals generate flat band near VBM that induces the high hole effective mass. The vanadium doped CCO shows the major contributions of Cu 3d orbitals similar to the pristine CCO however the O 2p orbitals shift towards the Fermi level and contribute to VBM. Further the V 3d orbital instead of Co 3d orbital dominates in both VBM and CBM. The O 2p contribution near VBM indicates the mixing of metal-oxygen (Cu-O) orbitals which is known as p-d hybridizations. The metal-oxygen overlap is good for higher p-type electrical conductivity. It can be seen from the band dispersion of CCVO (see Fig. 5.3(b)) that the bands are dispersive as compared to the pristine CCO, indicating the low hole effective mass. Overall, it is observed that the V doping in $CuCoO_2$ can enhance the p-type

conductivity as well as provide high hole mobility and hence a suitable material for ultrafast carrier dynamics.

5.3.3 Phonon Dispersion Curves and Raman Spectra

To identify the local crystal structures and bonding environments of the CCO, phonon dispersion curves (PDCs) are calculated and a detailed Raman spectroscopic analysis is performed. To validate our experimental Raman spectra, we have theoretically calculated the Raman spectra by density functional perturbation theory (DFPT). Experimental and theoretical Raman spectra of CCO are shown in Fig. 5.4 (a). It can be seen from Fig. 5.4(a) that there is a reasonable agreement between experimental and calculated Raman spectra. The primitive unit cell of delafossites contains four atoms that generate 12 phonon modes (see Fig. 5.4(b)). The vibrational modes of CCO can be summarized by the following irreducible representation at the zone center

$$\Gamma = A_{1g} + E_g + 3A_{2u} + 3E_u \qquad (5.1)$$

where symbols g, u and E respectively represent the Raman active, IR active and degenerated modes. There are two strong peaks observed in experimental as well as theoretical Raman spectra. The Raman spectra of delafossite type oxides show two Raman active modes namely E_g and A_{1g}. The E_g mode is a degenerate and arises due to the O-Co-O bending vibrational modes perpendicular to the c-axis (see right panel of Fig. 5.4) whereas, the A_{1g} mode arises at 710.23 cm^{-1} due to the parallel vibration of the metal-oxygen (Cu-O) bonds along c axis. The peak at 517.8 cm^{-1} in both experimental and theoretical Raman spectra is assigned to E_g modes. The Raman spectra of CCO show good agreement with the previously reported data [24, 25, 27-29]. The phonon dispersion curves along with the phonon density of states are shown in Fig. 5.4(b). The frequency of all phonon modes is real throughout the Brillouin zone (BZ) indicating the dynamical stability of CCO compounds. The Cu and Co atoms possess D_{3d} site symmetry; while, the oxygen occupy C_{3v} site symmetry. The CCO compounds allow D_{3d} site

symmetry at zone center. We have analyzed the symmetry of phonon patterns at the zone center and other high symmetry points along with the different directions of the BZ.

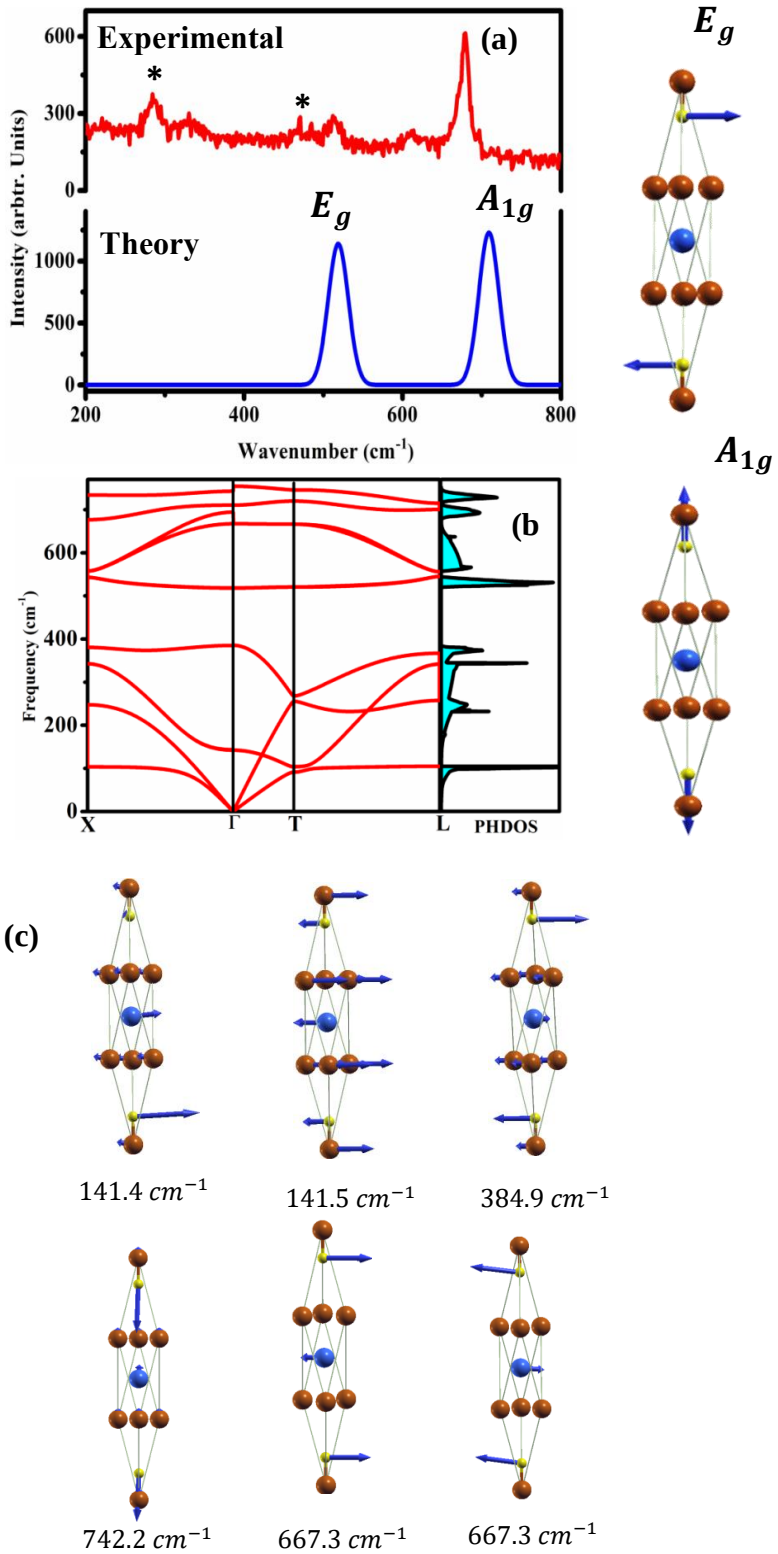

Figure 5.4: (a) Experimental and theoretical Raman spectra of pristine CCO compound (b) The phonon dispersion curves (PDCs) of CCO unit cell. Right panel of the graph shows the vibrational modes in perpendicular and parallel direction. (c) Phonon eigen vectors with the frequency of $CuCoO_2$ at zone center.

The high symmetry points other than the zone center give the following irreducible representations:

$$X = 2A_g + B_g + 3A_u + 6B_u \quad (5.2)$$

$$T = 2A_{1g} + 2E_g + 2A_{2u} + 2_{Eu} \quad (5.3)$$

$$L = 4A_g + 2B_g + 2A_u + 4B_u \quad (5.4)$$

$$\Gamma X = 8A' + 4A'' \quad (5.5)$$

$$\Gamma T = 4A_1 + 4E \quad (5.6)$$

$$\Gamma L = 8A' + 4A'' \quad (5.7)$$

The point group D_{3d} is a symmorphic group. The modes associated with the small representations have been chosen from corresponding point groups. In $CuCoO_2$, both Cu and Co atoms are situated at the site of maximal symmetry. At **Γ** and **T** points of the BZ, the even (g) modes originate due to the phase opposition vibrations of O atoms, however, at X point they show in-phase vibrations. At **Γ** and **T** points and along **Γ-T** direction of the BZ, the threefold axis (C_3) induces the classification of normal modes as A or E. "A" modes represent the vibration in the direction of the Cu—O bonds, whereas, double degenerate E modes imply the vibration in the perpendicular direction. At **X** point, the formation is originated by the two-fold axis (C_2) at the inversion center (i). The "A" modes are invariant while "B" modes change their sign under (C_2). In the even A_g mode, invariance concerning (C_2) indicates vibration in the σ plane whereas; the B_g mode shows the vibration along the two-fold axis (C_2). Along **Γ-T** and **Γ-X** directions of the BZ, the only symmetry operation σ takes place in terms of parallel A' and perpendicular A" modes. There is an overall similarity with symmetry operations with the previously reported delafossite compounds, however, they differ in sequence of phonon branches and their frequencies. The PDC (see Fig. 5.4(b)) of $CuCoO_2$ is less dispersive as

compared to other delafossite oxides indicating strong Cu-Co bonding. The eigenvector of phonon modes corresponding to their frequency are also shown in Fig. 5.4(c).

5.3.4 Magnetic Properties

The magnetic properties of pristine CCO and V doped CCO powders are determined at room temperature by a vibrating sample magnetometer (VSM) as shown in Fig. 5.5. A linear dependence of magnetization on the applied magnetic field revealed clear paramagnetic behavior for the $CuCoO_2$ and $CuCo_{1-x}V_xO_2$ (x = 0.06). Additionally, it is found that the variation of concentration of vanadium does not change the nature of magnetization. However, there is a slight change in magnetization values. The magnetization slightly varies with vanadium concentration (0.06) compared to the pristine CCO. A similar conclusion is drawn from the spin polarised DFT calculations that the vanadium concentration slightly increases the magnetization. It can be seen from Fig. 5.3 that the spin polarised electronic properties of V doped model is not identical, whereas, this is not true for pristine CCO. To understand this, an analysis with the ionic radii of Co^{3+} and V^{4+} is necessary. It is noted that the exhibited characteristics are similar to the delafossite group (space group: $R\bar{3}m$). In the delafossite structure, each Cu atom is linearly coordinated with two oxygen atoms, resulting in O-Cu-O dumbbells parallel to the c-axis to form layered triangular lattice anti-ferromagnets. Further, each oxygen in the O-Cu-O dumbbells is coordinated with three Co atoms parallel to the ab plane. The primary role of partial trivalent ions for Co^{3+} is to introduce a structural modulation in the triangular lattice. This leads to multiferroic phase formation [30]. We observe significant changes in the lattice parameters with increasing V content due to a difference in ionic radii of Co^{3+} and V^{4+} ions. The interaction of the trivalent (M^{3+}) cations through M–O–M linkages expected to be antiferromagnetic [31]. For low V contents, short-range interactions of Co–O–Co and Co–O–V are not affected, therefore, a paramagnetic regime could be obtained. Fig. 5.5 depicted that the hysteresises for CCO and CCVO (x = 0.06) are not much deviated. The M–H

hysteresises for other concentrations are not shown due to similar behavior. It is observed that the hysteresis curve is a little S-shaped and no magnetization saturation is obtained. This indicates the mixed effects on the magnetic properties of $CuCoO_2$ delafossite oxide at room temperature.

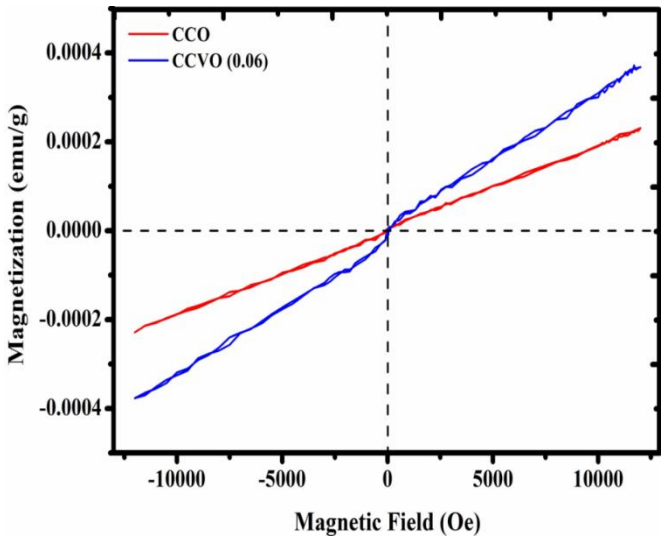

Figure 5.5: M–H curves of $CuCoO_2$ (CCO) and $CuCo_{1-x}V_xO_2$ (CCVO) (0.06)) powders measured at 300 K.

5.3.5 Optical Properties

After confirming the robust p-d hybridization near VBM from the PDOS and the inherent strength of the electronic properties of the CCO, we now turn our attention towards their optical properties. These properties provide momentous information about the interaction of light with the materials. The optical constants such as real and imaginary parts of a dielectric constant, absorption coefficients, refractive index, extinction coefficient, reflectivity, and loss spectra are calculated by the RPA method as described in Chapter 2.

A. Real Part $\varepsilon_1(\omega)$ and Imaginary Part $\varepsilon_2(\omega)$ of the Dielectric Function

The complex dielectric functions of pristine and vanadium doped CCO are shown in Fig. 5.6(a-b). It is seen that the behavior of $\varepsilon_1(\omega)$ is dissimilar due to the doping of vanadium (see Fig. 5.6(a-b)) in CCO. These compounds demonstrate the anisotropy except for the intermediary energies. It can be seen from Fig. 5.6(a-b) that the real part of the dielectric

constants reaches maxima at around 1.8 and 1.2 eV for pristine and doped CCO respectively. These maximum peaks of $\varepsilon_1(\omega)$ is directly attributed to the electronic transitions between the top of the valance band and the bottom of the conduction band. Moreover, the reduction in the electronic band gap results in the decrement in the magnitude of energy of these main peaks of $\varepsilon_1(\omega)$ [32]. Furthermore, for the energy where $\varepsilon_1(\omega) = 0$, in the ultraviolet region, indicates the absence of dispersion responsible for maximum absorption. The $\varepsilon_1(\omega) < 0$, nevertheless, indicates that the electromagnetic (EM) wave does not propagate, henceforth, the scrutinized materials can be utilized as a shield counter to the high EM wave [33-35]. The behavior of $\varepsilon_1(\omega)$ is unalike due to the diversity in the electronic properties of pristine and doped CCO. The peak intensity of pristine and doped CCO decreases due to the decrement in the electronic band gap i.e. from 1.03 to 0.40 eV. The conventional delafossites and chalcopyrites such as $CuAlO_2$, $CuMO_2$ (M = H, Li, Na, K, Rb), $CuMX_2$ (M = Ga, Al, In, Rh, B; X = S, Se, Te), etc. show the same nature of $\varepsilon_1(\omega)$, depending upon the electronic band gap [36-45]. The calculated imaginary part of a dielectric constant $\varepsilon_2(\omega)$ for pristine and doped CCO is undeniably linked to their electronic band structure which corresponds to the photon energy up to 10 eV and are shown in Fig. 5.7(a-b). Here, one observes the different behaviour or line shapes of $\varepsilon_2(\omega)$ for the considered compounds i.e. $CuCoO_2$ and $CuCo_{1-x}V_x$ due to their dissimilarities in the electronic band structure. The sharp peak in $\varepsilon_2(\omega)$ spectra originated mainly due to the hybridized bonding between Cu 3dand O 2p orbitals near VBM in $CuCoO_2$ and $CuCo_{1-x}V_x$ compounds. The fundamental absorption edge arises at 0.98 eV and 0.35 eV respectively for $CuCoO_2$ and $CuCo_{1-x}V_x$ compounds. These values are linked to their electronic band gap value, signifying the natural output of $\varepsilon_2(\omega)$ from the electronic band structure as shown in Fig. 5.7(a-b). The various interband electronic transitions are associated with the imaginary part of the dielectric function and the threshold of absorption occurs due to the direct electronic transition from the top of the valence band to the bottom of the conduction band.

The behaviour of $\varepsilon_2(\omega)$ spectra resemble the formerly studied p-type chalcopyrite and delafossite compounds [36-45].

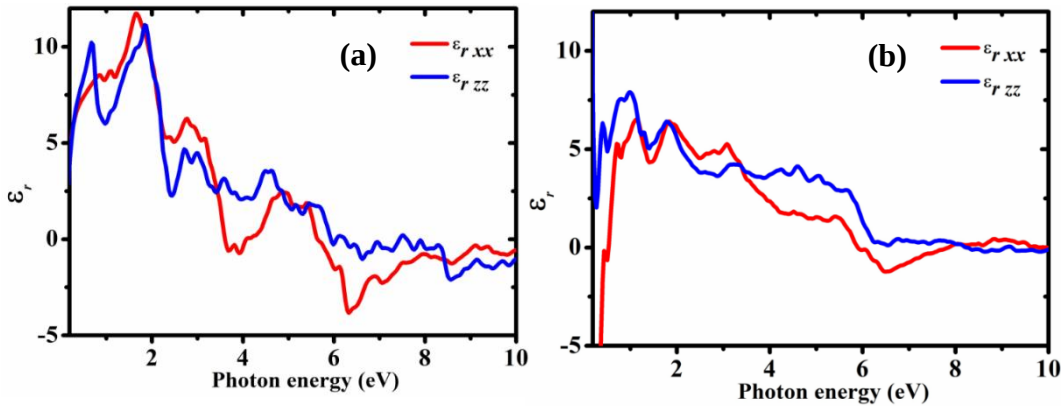

Figure 5.6: Real part of dielectric functions of (a) pristine CCO and (b) vanadium doped CCO.

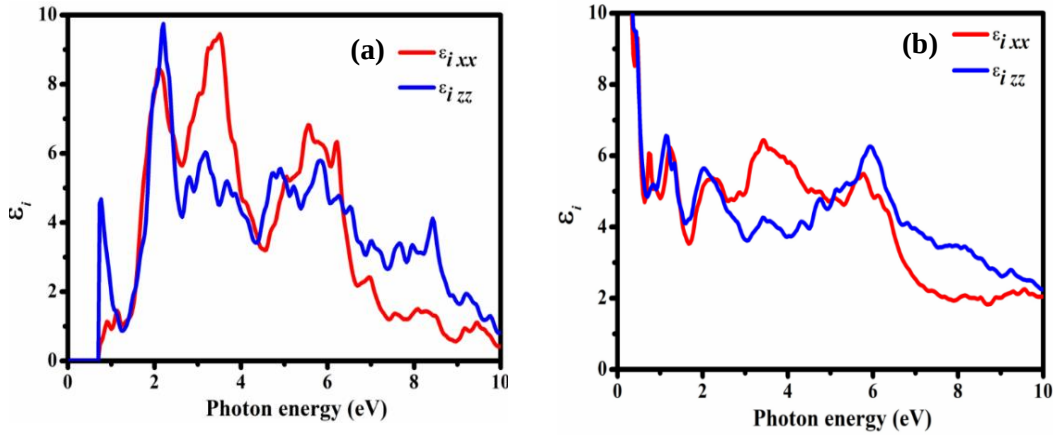

Figure 5.7: Imaginary part dielectric functions of (a) pristine CCO and (b) vanadium doped CCO.

B. Absorption Coefficient α (ω)

To have more insights into the possibilities of the considered compounds in the photovoltaic conversion applications, we have calculated absorption spectra $\alpha(\omega)$ corresponding to photon energy up to 10 eV and are displayed in Fig. 5.8(a-b). The absorptive nature of the material towards light is described by absorption coefficient $\alpha(\omega)$. Figure 5.8(a-b) indicates that all the perpendicular and parallel components of absorption coefficients are anisotropic. The opposite trend of these compounds is due to the robust

anisotropic behavior of these components with respect to the polarization of light. The threshold of absorption occurs at 1.0 eV for $CuCo_2$ and 0.25 eV for $CuCo_{1-x}V_x$ compounds. These compounds show a maximum peak in the ultraviolet region, suggesting the usefulness of these compounds in optoelectronics in the higher energy region (see Fig 5.8(a-b)). These threshold values are comparable with the nitride-based delafossites XYN_2 (X = Cu, Ag; Y = V, Nb, Ta) [45]. The other delafossites such as $CuAlO_2$, $CuGaO_2$, $AgScO_2$, $AgAlO_2$, and $AgCrO_2$ display the absorption edge within the range of 0.5 – 5 eV, which is comparable with the absorption edge of the considered compounds i.e. $CuCo_2$ and $CuCo_{1-x}V_x$ [46-50].

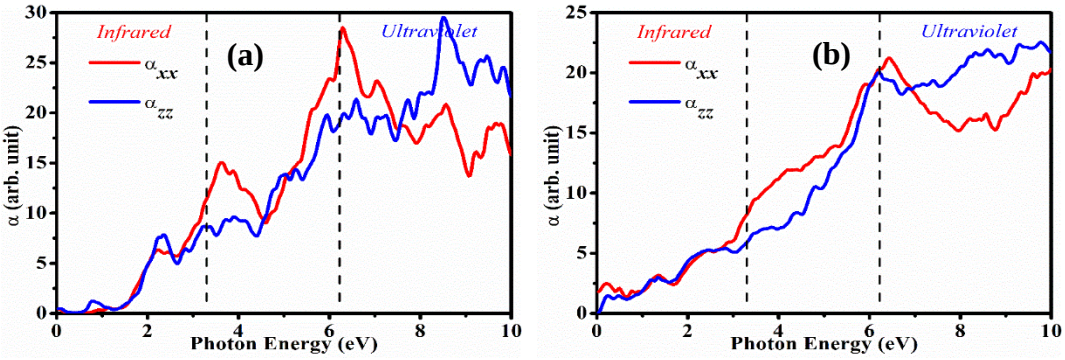

Figure 5.8: Absorption coefficient $\alpha(\omega)$ of (a) pristine CCO and (b) vanadium doped CCO.

C. Refractive index n(ω) and Extinction coefficient k(ω)

To confirm the potential applications of $CuCo_2$ and $CuCo_{1-x}V_x$ compounds in optoelectronics, we have performed the analysis of refractive index spectra $n(\omega)$ and presented them in the panels of Fig. 5.9(a-b). The electronic properties of these compounds further motivated us to calculate $n(\omega)$ to understand deeply the optical response of these scrutinized compounds. The calculated values of $n(\omega)$ are 1.65 and 4.45 for $CuCo_2$ and $CuCo_{1-x}V_xO_2$ respectively. Fig. 5.9(a-b) depicts that the doping of vanadium at the place of cobalt brings a drastic change in the peak intensity. The doping of vanadium does not only shift the parallel and perpendicular components toward the lower energy region but also decreases the peak intensity as we move from infrared to visible to the ultraviolet region($IR \rightarrow VI \rightarrow UV$). The

value of refractive index $n(\omega)$ is comparable with the formerly scrutinized compounds such as $CuInO_2$, $CuAlO_2$, and $CuScO_2$ [51-53]. The smaller ionic radii for vanadium doped copper-cobalt oxide results in an enormous refractive index value. In the infrared region, refractive index $n(\omega)$ increases further in the visible region, suggesting potential applications in the field of optoelectronics of $CuCoO_2$ compound, while, vanadium doped $CuCoO_2$ shows a remarkable peak in the infrared region. The extinction coefficient $k(\omega)$ shows how the oscillation amplitude decays with respect to the incident photon energy. All compounds have dissimilar behavior of parallel and perpendicular components of $k(\omega)$ due to the doping of vanadium as shown in Fig. 5.10(a-b). However, vanadium doped CCO shows a more intense peak in the perpendicular direction as compared to the pristine CCO because of the difference in the ionic radii (see Fig. 5.10(a-b)). The peak intensity increases in the higher energy region for pristine CCO, while, V doped CCO shows a less intense peak in the higher energy region. Furthermore, the magnitude of $k(\omega)$ increases with an increase in the photon energy. The coefficient of extinction decreases in the higher energy region (ultraviolet), signifying the decay of oscillation amplitude of the electric field.

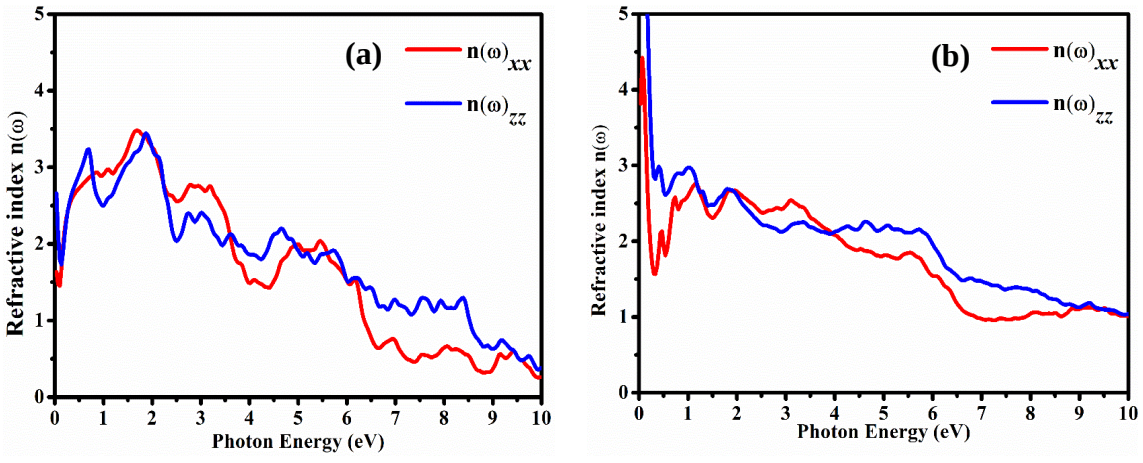

Figure 5.9: Refractive index n (ω) of (a) pristine CCO and (b) vanadium doped CCO.

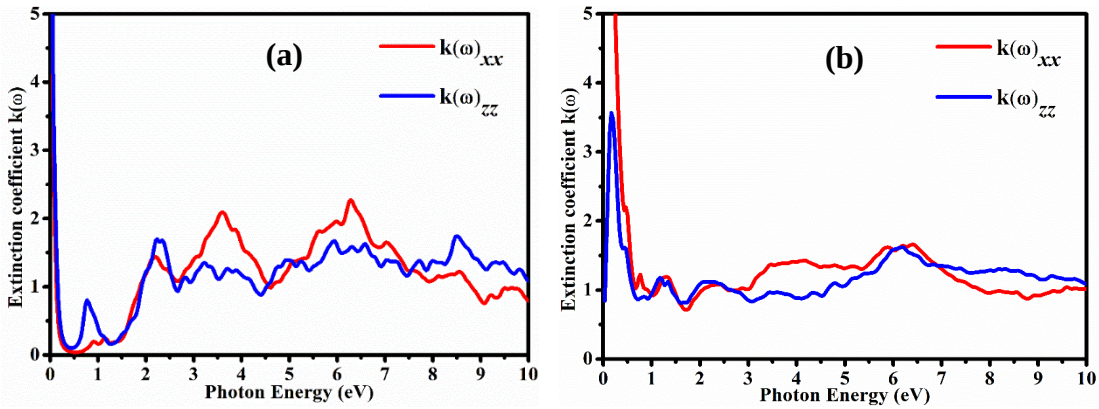

Figure 5.10: Extinction coefficient k (ω) of (a) pristine CCO and (b) vanadium doped CCO.

D. Optical reflectivity R(ω) and Loss spectrum L(ω):

Optical reflectivity spectra $R(\omega)$ is calculated corresponding to photon energy up to 10 eV along with the perpendicular and parallel components of the polarization as shown in Fig. 5.11(a-b). The doping of V at the place of Co decreases the magnitude of the peak intensity in the higher energy region. This decrement in the magnitude of peak intensity can be ascribed to the reduction in the band gap. The optical reflectivity of pristine CCO is maximum in the ultraviolet region, indicating the applicability of this compound as non-linear optical devices and Bragg reflectors [54].

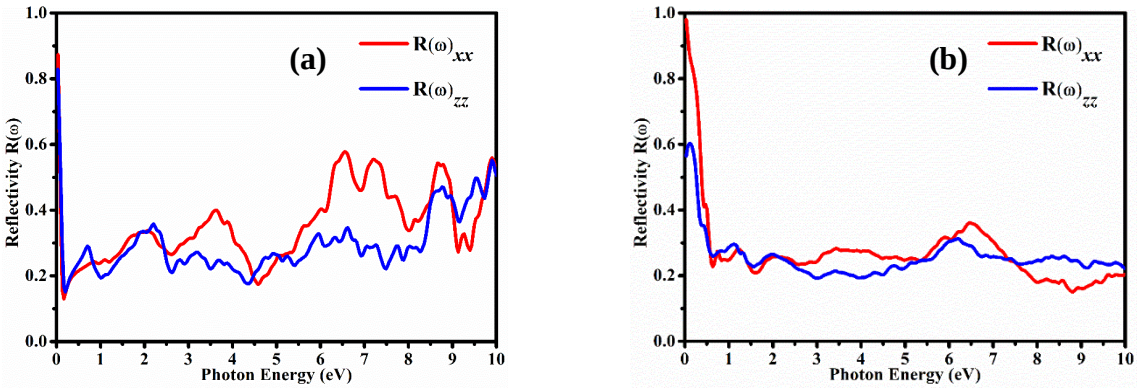

Figure 5.11: Optical reflectivity spectra of (a) CCO and (b)) vanadium doped CCO.

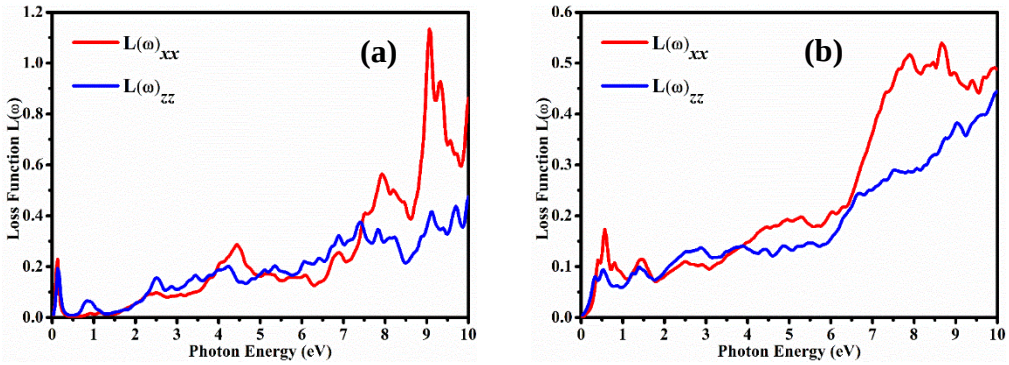

Figure 5.12: Energy loss spectra of (a) CCO and (b)) vanadium doped CCO.

Figure 5.12(a-b) displays the energy loss spectra $L(\omega)$ corresponding to photon energy up to 10 eV and is used to understand the energy loss by an electron when it passes through a homogeneous dielectric medium. Loss spectra increases from lower energy to higher energy (ultraviolet region) with a small difference in the magnitude of the peak intensity due to the difference in the electronic band structure, as mentioned above. The main peak in the energy loss spectrum of pristine CCO and V doped CCO can be attributed to the bulk plasma oscillation frequency ω_p, which is nothing but the collective excitation of loosely bound valence electrons in the conduction band, where the energy levels are vacant. Fig. 5.12(a-b) depicts a broad plasma peak associated with the strong hybridization between Cu 3d and O 2p orbitals near VBM. It is seen from Fig. 5.12(a-b) that the pristine and V doped CCO display sharp peaks at the higher energy region, mostly ultraviolet region, indicating fast energy loss of an electron in this region. The energy loss by an electron in the higher energy region for pristine CCO is more as compared to the V doped CCO. However, the loss of an electron in the visible region for both these considered compounds is less, indicating the potential applications in optoelectronic devices.

5.4 Conclusions

This work presents a combined experimental and theoretical investigation on structural electronic, vibrational and magnetic properties of $CuCoO_2$, and its V doped $CuCoO_2$ at

different concentrations. The XRD diffraction patterns confirm the pure rhombohedral phase formations of pristine CCO and V doped CCO. The phase formation and bonding environments were further analyzed by Raman and XPS spectroscopy. The V prefers the tetravalent occupancy (V^{+4}) when doped at the Co site. The VBM modulation is observed during V doping due to higher metal-oxygen overlap. The pristine CCO compound shows an indirect band gap of 1.03 eV, however, it reduces to 0.40 eV when doped with V atoms. Furthermore, we report a study of the magnetic properties of delafossite CCO and CCVO by a vibrating sample magnetometer (VSM). The pristine CCO and V doped CCO compounds show paramagnetic behavior. The V doping slightly increases the magnetization values confirmed by the theoretical calculations. The magnetic properties of these compounds also depend on the ionic radii of trivalent atoms. The electronic band structure and the PDOS of these compounds indicated the p-d hybridization induced by the V doping. The p-d hybridization observed in V doped CCO indicates that the substitution of V at the Co site generates more free holes which is good for better p-type conductivity. The results of dielectric constant and absorption coefficient of pristine and V doped CCO indicate that these compounds can be used in optoelectronicapplications. Refractive index spectra increase in the visible region and the reflectivity spectra show maximum peaks in the ultraviolet region, and the loss spectra indicate the least energy loss by an electron in the visible region, confirming potential applications of these compounds in optoelectronic applications.

References

1. I. Sinnarasa, Y. Thimont, L. Presmanes, A. Barnabé, P. Tailhades, *Nanomaterials.*, **7,** 157 **(**2017).
2. M. Yu, G. Natu, Z. Ji, Y. Wu, *J. Phys. Chem. Lett.*, **3,** 1074 **(**2012).
3. A. K. Diaz-Garcia, T. Lana-Villarreal, R. Gomez, *J. Mater. Chem. A.*, **3,** 19683 (2015).
4. A. B. Garg, R. Rao, *Crystals*, **8**, 255 (2018).
5. E. Fortunato, R. Martins, *Phys. Status Solidi*, **5,** 336 **(**2011).

6. E. Fortunato, R. Barros, P. Barquinha, V. Figueiredo, S.-H. K. Park, C.-S. Hwang, R. Martins, *Appl. Phys. Lett*., **97,** 052105 (2010).
7. H. Kawazoe, M. Yasukawa, H. Hyodo, M. Kurita, H. Yanagi, H. Hosono, *Nature,* **389,** 939 (1997).
8. R. Nagarajan, A. D Draeseke, A.W. Sleight, J. Tate, *J. Appl. Phys.*, **89,** 8022 (2001).
9. J. F. H. L Monteiro, F. C. Monteiro, A. R. Jurelo, D. H. Mosca, *Ceramics International.*, **44,** 14101 (2018).
10. H. Gong, Y. Wang, Y. Luo, *Appl. Phys. Lett*., **76,** 3959 (2000).
11. E. Schiavo, C. Latouche, V. Barone, O. Crescenzi, B. M. Garcíad, M. Pavone, *Phys. Chem. Chem. Phys*, **20,** 14082 (2018).
12. R. Nagarajan, N. Duan, M. K. Jayaraj, J. Li, K. A. Vanaja, A. Yokochi, A. Draeseke, J. Tate, A. W. Sleight, *Int. J. Inorg. Mater.*, **3,** 265 (2001).
13. D. O. Scanlon, G. W. Watson, *J. Mater. Chem*., **21,** 3655 (2011).
14. M. A. Marquardt, N. A. Ashmore and D. P. Cann, *Thin Solid Films.*, **496,** 146 (2006).
15. T. F. Cerqueira, S. Lin, M. Amsler, S. Goedecker, S. Botti, M. A. Marques, *Chem. of Mat*., **27,** 4562 (2015).
16. D. Upadhyay, A. Pratap, P. K. Jha, *J. Raman Spectrosc*., **50**, 603 (2019).
17. J. S. Kang, J. H. Kwak, Y. J Shin, S. W. Han, K. H Kim, B. I. Min, *Phys. Rev. B.*, **61,** 10682 (2000).
18. D. Shin et al., *Phys. Rev. B.*, **80,** 233105 (2009).
19. A. Garg, A. Mishra, K. Pandey, S. Sharma, *J. Appl. Phys.*, **116,** 133514 (2014).
20. P. Giannozzi, et al., *J. Phys. Condens. Matter*., **21,** 395502 (2009).
21. J. P. Perdew, K. Burke, M. Ernzerhof, *Phys. Rev. Lett.*, **77**, 3865 (1996).
22. 26J. D. Pack, H. J. Monkhorst, *Phys. Rev. B.*, **16**, 1748 (1977).
23. S. Baroni, S. de Gironcoli, A. Dal Corso, P. Giannozzi, *Rev. Mod. Phys.*, **73**, 515 (2001).
24. Qian, T. Zhang, J. Bai, D. Fang and H. Li, Dalton Trans., **48**, 13759 (2019).
25. Z. Du, J. Qian, J. Bai, H. Li, M. Wang, X. Zhao, D. Xiong, *Inorg. Chem.*, **59,** 9889 (2020).
26. D. Kim, M. Kim, J. Yi, S. H. Nam, J. H. Boo, Y. S. Park, J. Lee, *Sci. Adv. Mater*., **9**, 8 (2017).
27. A. B. Garg, R. Rao, *Crystals*., **8**, 255 (2018).
28. T. Elkhouni M. Amami, P. Strobel, A. Ben salah J. Supercond. Nov. Magnet., 26, 2802 (2013).
29. D. Xiong, Z. Du, H. Li, J. Xu, J. Li, X. Zhao, L. Liu, *ACS Sustain. Chem. Eng.*, **7**, 1501 (2019).

30. L. Naka-in, T. Kamwanna, P. Srepusharawoot, S. Pinitsoontorn, V.Amornkitbamrung, *Jpn. J. Appl. Phys*., **54**, 04DH10 (2015).
31. T. Elkhouni, M. Amami, C.V. Colin, P. Strobel, A. Ben Salah, *J. Magn. Magn. Mater*., **330**, 101 (2013).
32. S. Saha, T. P. Sinha, A. Mookerjee, *Phys. Rev. B.*, **62**, 8828 (2000).
33. Y. Li, W. Fan, H. Sun, X. Cheng, P. Li, X. Zhao, *J. Appl. Phys.*, **109**, 113535 (2011).
34. R. D. L. Kronig, *J. Opt. Soc. Am.*, **12**, 547 (1926).
35. A. Shankar, R. Thapa, P. Mandal, *J. Phys. Conf. Ser.*, **765**, 012008 (2016).
36. A. Sajid, S. Ullah, G. Murtaza, R. Khenata, A. Manzar, S. B. Omran, *J. Optoelectron. Adv. Mater.*, **16**, 76 (2014).
37. M. V. Yakushev, F. Luckert, C. Faugeras, A. V. Karotki, A. V. Mudryi, and R. W. Martin, *Appl. Phys. Lett.*, **97**, 152110 (2010).
38. A. S. Verma and D. Sharma, *Phys. Scr*., **76**, 22 (2007).
39. S. Bagci, B. G. Yalcin, H. A. R. Aliabad, S. Duman, B. Salmankurt, *RSC Adv*., **6,** 59527 (2016).
40. H. Salehi, E. Gordanian, *Mater. Sci. Semicond. Process*., **47**, 51 (2016).
41. N. Joshi, D. Upadhyay, A. Pandya and P. K. Jha, *J. Appl. Phys*., **126**, 235705 (2019).
42. R. Singh, R. K. Ulrich, *Electrochem. Soc. Interface*, **8**, 26 (1999).
43. Y. Wang, W. Liu, H. Chen, X. Chen, C. Liu, G. Zhuang, R. Wang, F. Shen, H. Wang, H. Xiaoyan, Z. Miao, *Phys. B.*, **545**, 167 (2018).
44. D. Upadhyay, N. Joshi, A. Pratap, P. K. Jha, *J. Appl. Phys*., **128**, 155701 (2020).
45. N. J. Szymanski, L. N. Walters, O. Hellman, D. Gall, and S. V. Khare, *J. Mater. Chem. A*, **6**, 20852 (2018).
46. M. Kumar, H. Zhao, C. Persson, *Semicond. Sci. Technol*., **28** 065003 (2013).
47. M. Choi, S. Yagi, Y. Ohta, K. Kido, T. Hayakawa, *J. Phys. Chem. Solid*, **150,** 109845, (2021).
48. K. C. Bhamu, J. Sahariya, R. Vyas, K. R. Priolkar, *Pramana*., **89**, 11 (2017).
49. K. C. Bhamu, K. R. Priolkar, *Mater. Chem. Phys*., **190**, 114 (2017).
50. A. A. H. El-Bassuony, H. K. Abdelsalam, *J. Mater. Sci. Mater. Electron*., **29**, 5401 (2018).
51. M. N. Spallart, S. P. Pai, R. Pinto, *Thin Solid Films.*, **515**, 8641 (2007).
52. C. W. Teplin, T. Kaydanova, D. L. Young, J. D. Perkins, D. S. Ginley, A. Ode, D. W. Readey, *Appl. Phys. Lett*., **85**, 3789 (2004).
53. J. P. Porres, A. Segura, D. Kim, *Semicond. Sci. Technol*., **24**, 015002 (2009).
54. B. G. Kim, E. Garmire, S. G. Hummel, P. D. Dapkus, *Appl. Phys. Lett*., **54**, 1095 (1989).